Earth and Planetary Science Letters 426 (2015) 58–68

Contents lists available at ScienceDirect

Earth and Planetary Science Letters

www.elsevier.com/locate/epsl

An 800-kyr record of global surface ocean $\delta^{18}O$ and implications for ice volume-temperature coupling

Jeremy D. Shakun [a,*], David W. Lea [b], Lorraine E. Lisiecki [b], Maureen E. Raymo [c]

[a] Department of Earth and Environmental Sciences, Boston College, Chestnut Hill, MA 02467, United States
[b] Department of Earth Science, University of California, Santa Barbara, CA 93106, United States
[c] Lamont-Doherty Earth Observatory, Columbia University, Palisades, NY 10964, United States

ARTICLE INFO

Article history:
Received 12 January 2015
Received in revised form 4 May 2015
Accepted 22 May 2015
Available online xxxx
Editor: H. Stoll

Keywords:
marine oxygen isotope record
glacial cycles
Pleistocene
ice volume
global temperature

ABSTRACT

The sequence of feedbacks that characterized 100-kyr glacial cycles of the past million years remains uncertain, hampering an understanding of the interconnections between insolation, ice sheets, greenhouse gas forcing, and climate. Critical to addressing this issue is an accurate interpretation of the marine $\delta^{18}O$ record, the main template for the Ice Ages. This study uses a global compilation of 49 paired sea surface temperature-planktonic $\delta^{18}O$ records to extract the mean $\delta^{18}O$ of surface ocean seawater over the past 800 kyr, which we interpret to dominantly reflect global ice volume. The results indicate that global surface temperature, inferred deep ocean temperature, and atmospheric CO_2 decrease early during each glacial cycle in close association with one another, whereas major ice sheet growth occurs later in glacial cycles. These relationships suggest that ice volume may have exhibited a threshold response to global cooling, and that global deglaciations do not occur until after the growth of large ice sheets. This phase sequence also suggests that the ice sheets had relatively little feedback on global cooling. Simple modeling shows that the rate of ice volume change through time is largely determined by the combined influence of insolation, temperature, and ice sheet size, with possible implications for the evolution of glacial cycles over the past three million years.

© 2015 Elsevier B.V. All rights reserved.

1. Introduction

The late Pleistocene glacial cycles provide an opportunity to explore linkages between components of the climate system, ice sheet behavior, and Earth system sensitivity to greenhouse-gas forcing. The SPECMAP group first articulated a strategy to address these questions over two decades ago (Imbrie et al., 1989). They capitalized on the then-recent discovery that glacial cycles are ultimately due to orbital forcing (Hays et al., 1976) and proposed that identification of the sequence of processes unfolding from this initial forcing would reveal the causal links responsible for pulling the world into and out of Ice Ages. This approach has borne fruit for the last deglaciation and suggests that increasing Northern Hemisphere summer insolation initiated ice melt, with the resulting meltwater forcing causing a reduction of the Atlantic Meridional Overturning Circulation strength (He et al., 2013). This reduction resulted in warming in the Southern Hemisphere via the bipolar seesaw, and the ensuing CO_2 rise, along with the continued increase of Northern Hemisphere summer insolation, led to global-scale warming and deglaciation (Denton et al., 2010; Shakun et al., 2012). On the other hand, the timing of events within the glaciation phase, which spans ~90% of the 100-kyr cycle, is less certain for two main reasons. First, weaker dating control further back in time makes it more difficult to assess phase relationships among different climate components and regions. Second, ice-sheet variations cannot be directly constrained on land, since evidence of their earlier extent was later scraped away by advancing ice. As a result, the marine $\delta^{18}O$ record from foraminiferal calcite ($\delta^{18}O_c$) is typically used to infer the record of glaciation. This record, however, reflects the combined signal of global ice volume and ocean temperature changes which have to be disentangled in order to understand ice sheet-climate coupling.

Several approaches have been applied previously to this problem. These include: measuring benthic foraminiferal isotopes ($\delta^{18}O_b$) at locations near the freezing point of water and thus in locations unable to cool further during glacials (Labeyrie et al., 1987); calibrating marine $\delta^{18}O_c$ against sea level benchmarks over the past glacial cycle and extending this relationship to previous cycles (Waelbroeck et al., 2002); measuring seawater $\delta^{18}O$ ($\delta^{18}O_{sw}$) directly from Last Glacial Maximum (LGM)-age pore flu-

* Corresponding author.
E-mail address: jeremy.shakun@bc.edu (J.D. Shakun).

http://dx.doi.org/10.1016/j.epsl.2015.05.042
0012-821X/© 2015 Elsevier B.V. All rights reserved.

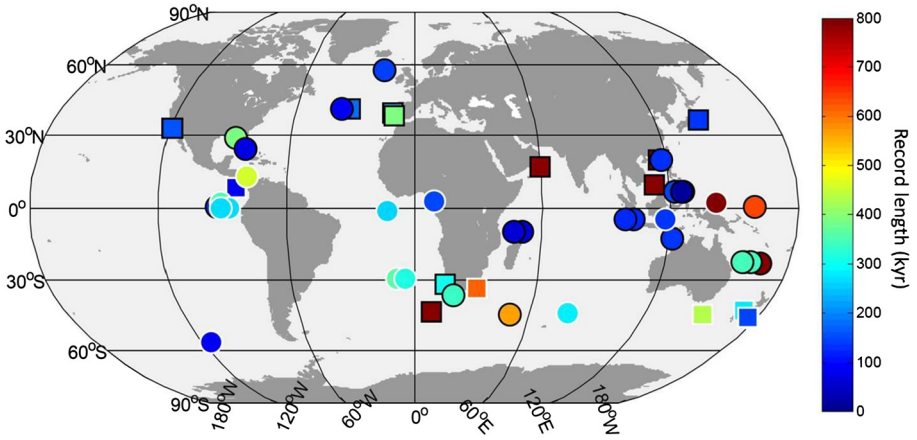

Fig. 1. Map showing the distribution of sites used in this study. Symbol shape denotes SST proxy type (circle = Mg/Ca, square = $U^{K'}_{37}$), symbol color represents how much time the record spans (see scale bar), and symbol outline color signifies age model type (black = $\delta^{18}O_b$, white = $\delta^{18}O_p$).

ids (Schrag et al., 2002); pairing the marine isotope record with the isotopic record of atmospheric oxygen from ice cores to deconvolve the ice volume component common to both (Shackleton, 2000); and lastly, inverse climate-ice sheet modeling motivated by the logic that both ice volume and deep ocean temperature are linked to high latitude temperature (Bintanja et al., 2005). Another avenue of research has taken the approach of independently measuring the temperature influence on the calcite record using the Mg/Ca proxy, and then subtracting this signal from the co-occurring $\delta^{18}O_c$ record to leave the $\delta^{18}O_{sw}$ component as the residual. This technique, which has been applied to individual benthic ostracode (Dwyer et al., 1995) and foraminifera records (Elderfield et al., 2012; Martin et al., 2002; Sosdian and Rosenthal, 2009), takes advantage of the more uniform properties of the deep ocean to minimize local overprints. However, the full potential of this technique is constrained by the lower sensitivity of Mg/Ca at colder bottom water temperatures as well as the small number of sites investigated so far. Lea et al. (2002) applied this approach to the warm surface ocean using a single planktic record from the eastern Equatorial Pacific. They acknowledged the possibility of local hydrological influences and suggested that "the solution to this problem is to construct a stack of $\delta^{18}O_{water}$ and sea surface temperature." Here we present such stacks for the last 800 kyr.

2. Data and methods

2.1. Stacking

We compiled a total of 49 paired planktonic $\delta^{18}O$-sea surface temperature ($\delta^{18}O_p$-SST) records from the global oceans (Fig. 1, Supplementary Table S1). Nearly all records span the last glacial cycle with an average resolution of 1.5 kyr, but the dataset degrades to only 7 records and 5-kyr mean resolution by 800 ka. Age models for cores not already on the LR04 time scale (Lisiecki and Raymo, 2005) were derived by correlating $\delta^{18}O_c$ to the LR04 stack with the program Match (Lisiecki and Lisiecki, 2002) using $\delta^{18}O_b$ if available ($n = 29$) or $\delta^{18}O_p$ if not ($n = 19$). One record spanning just the last 57 kyr was left on its radiocarbon and ice-core tuned age model (MD98-2181). The majority of SST records are based on the Mg/Ca of surface or near-surface dwelling foraminifera ($n = 34$), which have the virtue of also being the carrier of the $\delta^{18}O_p$ signal, but some alkenone-based SST records were also included ($n = 15$). Five cores have paired Mg/Ca-$\delta^{18}O_p$ records measured on two different species, which we treat as independent records. We used the published SST reconstructions, regardless of the original authors' choice of proxy-SST calibration. SST and $\delta^{18}O_p$ records were first interpolated to 3-kyr resolution by averaging data points in non-overlapping 3-kyr bins, and then $\delta^{18}O_{sw}$ was calculated on a record-by-record basis using the equation: $\delta^{18}O_{sw}(\text{VSMOW}) = 0.27 + (\text{SST}(^\circ\text{C}) - 16.5 + 4.8 \times \delta^{18}O_p(\text{VPDB}))/4.8$ (Bemis et al., 1998). To produce stacks, individual SST and $\delta^{18}O_{sw}$ records were shifted to a mean of zero and combined as unweighted global averages (Fig. 2). We considered using the longest records in order to define the long-term trends, which could be used to adjust the means of the shorter records before stacking, but this made negligible difference to the final stacks. Likewise, statistically filling in data gaps in the longest records made little difference to the appearance of the stacks.

2.2. Sensitivity tests

The sensitivity of the $\delta^{18}O_{sw}$ stack to regional differences and potential proxy or chronological biases in the dataset was tested by calculating $\delta^{18}O_{sw}$ stacks for various data subsets based on latitude, hemisphere, ocean basin, proxy type, and chronology (Fig. 3). The various stacks agree quite well over the last 200 kyr, suggesting that the planktic stacking approach yields robust results when applied to a sufficient number of widely distributed records. The correlations among the stacks generally decrease further back in time, probably due to the decreasing number of records, though general similarities are still apparent.

2.3. Uncertainty analysis

We calculated uncertainties in the $\delta^{18}O_{sw}$ stack in two ways. First, we used the approach of Gibbons et al. (2014), propagating uncertainties in the $\delta^{18}O$-paleotemperature equation, Mg/Ca-SST calibration, and Mg/Ca and $\delta^{18}O$ measurements, and obtained 1σ errors that increase from 0.06 to 0.18‰ with age of the $\delta^{18}O_{sw}$ stack due to the declining number of records in the older intervals. Second, we calculated the standard error of $\delta^{18}O_{sw}$ records, which increases with age from 0.05 to 0.12‰ (1σ). We prefer the latter estimate because it reflects the degree of covariance among $\delta^{18}O_{sw}$ records, and thus provides an indication as to how well the stack may represent the global average. In addition, absolute errors in the $\delta^{18}O$-paleotemperature equation and proxy-SST calibrations have less relevance to the stack because the stack is only concerned with relative changes. The glacial–interglacial range in the $\delta^{18}O_{sw}$ stack across the last two terminations, discussed below, was quantified as the difference between the first and last datapoints on the abrupt deglacial transitions, and the uncertainty

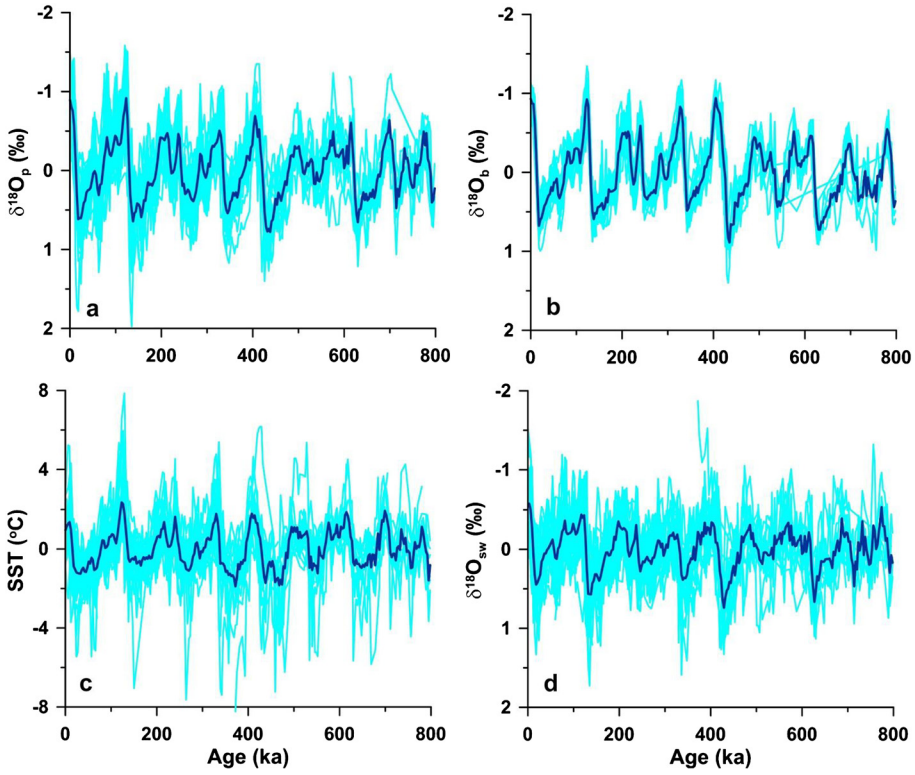

Fig. 2. Individual (cyan) and stacked (blue) records for (**a**) $\delta^{18}O_p$, (**b**) $\delta^{18}O_b$, (**c**) SST, and (**d**) $\delta^{18}O_{sw}$ (i.e., SST-corrected $\delta^{18}O_p$). All records have been shifted to a mean of zero. (For interpretation of the references to color in this figure legend, the reader is referred to the web version of this article.)

on this estimate was taken from the standard errors on the datapoints combined in quadrature.

2.4. Significance of correlations

All time series correlations reported below are significant at the 95% confidence level or higher, calculated by conservatively assuming that the effective degrees of freedom in the time series correspond to the number of cycles they contain. For instance, Neff of global SST over the past 800 kyr was taken as eight, corresponding to the number of glacial cycles during this interval, while Neff of the summer energy forcing was taken to be 20 since it is dominated by 41 kyr obliquity cycles.

3. Global $\delta^{18}O_{sw}$ and SST stacks

3.1. The last glacial cycle

There is modest regional variability in individual $\delta^{18}O_{sw}$ records for the last glacial cycle (e.g. $\delta^{18}O_p$ records with independently-derived SST effects removed) (Fig. 4). For instance, Atlantic records tend to exhibit a slightly larger glacial–interglacial range as well as greater orbital-scale variability, such as a stronger MIS 5–4 transition, than records from the Indo-Pacific. Overall, however, there is notable global coherency in both amplitude and structure (Fig. 4). Indeed, a principal components analysis indicates that 71% of the variance in high-resolution records covering the last glacial cycle can be explained by a single mode of variability that approximates the global mean. Furthermore, the glacial–interglacial difference across the last two terminations in the global $\delta^{18}O_{sw}$ stack is 1.0 ± 0.08‰ (Fig. 4), which is in close agreement with deep-ocean estimates of 1.0 ± 0.1‰ based on LGM pore fluids (Schrag et al., 2002). In addition, the $\delta^{18}O_{sw}$ stack closely resembles the sea-level record of the last glacial cycle from coral benchmarks (Medina-Elizalde, 2013) (Fig. 4). We take these three observations – that $\delta^{18}O_{sw}$ varied in general harmony around the surface ocean, that it was similar in magnitude to deep ocean changes, and that it tracked sea level – to imply that the $\delta^{18}O_{sw}$ stack largely reflects the changing isotopic composition of the whole ocean, and thus ice volume variability. This global coherency is noteworthy especially given that (1) the glacial–interglacial ranges in the component SST and $\delta^{18}O_p$ records vary from 2.8 to >10 °C and 1.1 to 3.4‰ (Fig. 2a, c), (2) local hydrological changes also overprint the global surface $\delta^{18}O_{sw}$ signal, (3) changes in meridional vapor transport can decouple surface ocean $\delta^{18}O_{sw}$ variability from the deep ocean by redistributing freshwater between the lower latitudes and sites of deepwater formation (Mix, 1992), and (4) proxy and age model differences add noise to the individual records. Despite these influences, the uniformity of the $\delta^{18}O_{sw}$ signal argues strongly for a dominant global ice volume control. With this interpretive framework in mind, we turn to the record of the last 800 kyr.

3.2. The last 800 kyr

The $\delta^{18}O_{sw}$ stack shows strong 100-kyr cycles over the past 800 kyr, and curiously, there is a gradual trend in the mean toward more negative values since 400 ka (Fig. 5b), related to weak interglacials in $\delta^{18}O_p$ during Marine Isotope Stages (MIS) 9 and 11 as well as 400-kyr amplitude modulations of SST (Fig. 2a, b). Because benchmarks firmly establish that sea level was likely >6 m higher during MIS 5e and 11 than during the Holocene (Dutton and Lambeck, 2012; Raymo and Mitrovica, 2012), this trend in the data cannot reflect ice volume. It is also unlikely to be caused by decreasing data resolution with age as similar 'upward' trends have been previously noted in individual $\delta^{18}O_{sw}$ records (Lea et al., 2002). Speleothems from Nevada and Borneo also exhibit similar trends (Meckler et al., 2012; Winograd et al., 1992), suggesting that these features may represent a large-scale hydrological signal.

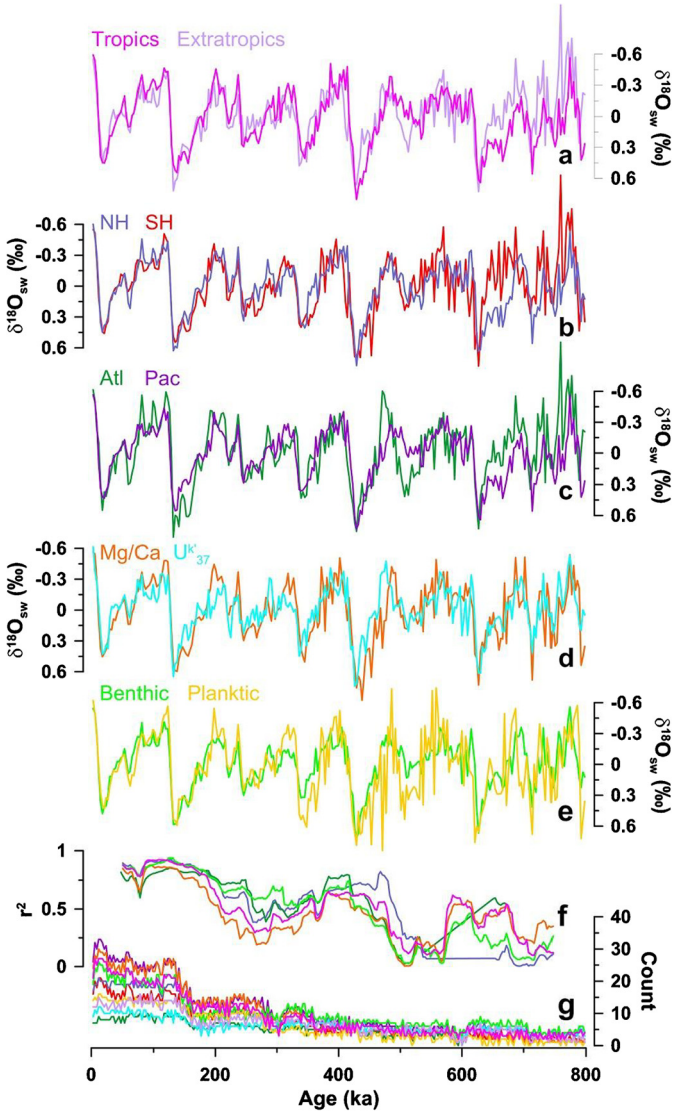

Fig. 3. $\delta^{18}O_{sw}$ stacks calculated for various subsets of the dataset, including the (**a**) tropics (23.5° S to 23.5° N) and extratropics (>23.5°), (**b**) Northern and Southern Hemisphere, (**c**) Atlantic and Pacific–Indian basins, (**d**) Mg/Ca and $U^{K'}_{37}$ records, and (**e**) records with age models based on $\delta^{18}O_p$ and $\delta^{18}O_b$. (**f**) The 100-kyr running correlation between the various pairs of stacks, represented by the color of the first stack shown in a–e. (**g**) The number of records contributing to each stack. All $\delta^{18}O_{sw}$ records have been shifted to have a mean of zero. The general correspondence between the various pairs of time series suggests that the $\delta^{18}O_{sw}$ reconstruction is not strongly sensitive to the location and type of component records, though some notable differences stand out such as the subdued MIS 11, 9, 7, and 5 interglacials in the stacks based on $\delta^{18}O_b$ chronologies and $U^{K'}_{37}$ records.

However, foraminiferal calcite diagenesis as a potential alternative explanation cannot be ruled out.

This modest long-term trend notwithstanding, a comparison of the stacked SST and $\delta^{18}O_{sw}$ records reveals a consistent and striking pattern over glacial cycles for the past 800 kyr; SST tends to cool during the first half of each cycle, while major $\delta^{18}O_{sw}$ enrichment does not occur until later in the cycle (Fig. 5b). Examination of the local SST-$\delta^{18}O_{sw}$ phase relationship for individual records shows that, while considerable variability exists, $\delta^{18}O_{sw}$ lags SST at 88% of sites at the precession frequency, at 86% of sites at the obliquity frequency, and at all sites at the eccentricity frequency (Fig. 6). We take the consistency of this phase lag as strong evidence that global $\delta^{18}O_{sw}$ and ice volume lags surface temperature at all orbital frequencies, and that this result is not sensitive to spatial or proxy biases. Furthermore, this interpretation rests on firm chronological footing because the $\delta^{18}O_{sw}$ and SST reconstructions are derived from the same sediment cores, all of which have been placed on the same timescale. This timing offset was already well-known for deep water temperatures during the last glacial cycle (Labeyrie et al., 1987; Waelbroeck et al., 2002) and has been found in modeling (Bintanja et al., 2005) and individual records (Elderfield et al., 2012; Lea et al., 2002) spanning older glacial cycles. The global dataset presented here demonstrates that a pronounced ice volume lag behind global surface temperature is a robust feature of late Pleistocene glacial cycles.

If $\delta^{18}O_{sw}$ derived from the planktonic compilation approximately mirrors deep ocean changes in $\delta^{18}O_{sw}$, subtracting this component from the LR04 benthic stack should yield the bottom water temperature component of benthic $\delta^{18}O$ ($\delta^{18}O_{bwt}$). Calculation of $\delta^{18}O_{bwt}$ suggests that deep ocean temperature varied in close association with global SST ($r^2 = 0.72$) as well as Antarctic air temperature inferred from ice cores ($r^2 = 0.73$) (Jouzel et al., 2007) (Fig. 7a, b). The latter connection perhaps reflects the Southern Ocean temperature signal imprinted on southern-sourced deep waters and the expansion and contraction of Antarctic Bottom Water over glacial cycles. The SST and bottom water temperature reconstructions are all also strongly correlated with atmospheric CO_2 ($r^2 = 0.49$ with SST and $r^2 = 0.59$ with bottom water temperature) (Luthi et al., 2008) (Fig. 7a, b).

3.3. Converting the $\delta^{18}O_{sw}$ stack to sea level

The long-term trend in the $\delta^{18}O_{sw}$ stack indicates that it contains a component unrelated to ice volume, and thus implies that surface ocean $\delta^{18}O_{sw}$ partially diverges from global ocean average $\delta^{18}O_{sw}$, at least on these longer time scales. Indeed, a comparison of $\delta^{18}O_p$ and $\delta^{18}O_b$ stacks from the sites used in this study suggests a similar long-term decoupling between the surface and deep ocean (Fig. 8a). In particular, the difference between these stacks shows a trend toward a more enriched surface ocean relative to the deep ocean from the beginning of the record at 800 ka to Termination V (430 ka), followed by an opposing trend from Termination V to the present (Fig. 8b).

As a first attempt to correct the $\delta^{18}O_{sw}$ stack for these non-ice volume effects, we removed these $\delta^{18}O_b - \delta^{18}O_p$ trends from the $\delta^{18}O_{sw}$ stack (Fig. 8c). This is an admittedly simple, ad hoc adjustment, but it is superior to detrending the $\delta^{18}O_{sw}$ stack itself and provides a starting point to consider the sea level signal contained in the $\delta^{18}O_{sw}$ stack; it also brings the stack into closer alignment with other sea level records (see below). We then scaled the detrended stack to sea level such that the Holocene is pinned at 0 m and the LGM is at −130 m (Fig. 8c) (Lambeck et al., 2014). This scaling implies a ratio of 0.008‰ per meter sea level, in agreement with pore waters for the LGM (Adkins et al., 2002).

3.4. Comparison to other sea level records

Existing $\delta^{18}O_{sw}$ and sea level reconstructions are, in general, broadly similar to each other as well as to our new reconstruction, with all recording a dominant 100 kyr ice-age cycle punctuated by abrupt terminations, as well as intervals of ice growth later in the glacial cycle than would be suggested by the raw marine $\delta^{18}O_c$ record (Fig. 9). This late timing for ice growth is most pronounced in the planktic $\delta^{18}O_{sw}$ stack; lag correlations suggest that it lags all of the other reconstructions, trailing the Waelbroeck et al. (2002), Bintanja et al. (2005), and Elderfield et al. (2012) reconstructions by ~2 to 3 kyr, and the Rohling et al. (2009) and Rohling et al. (2014) reconstructions by ~6 kyr. The Red Sea and Mediterranean sea level reconstruction method corrects for local

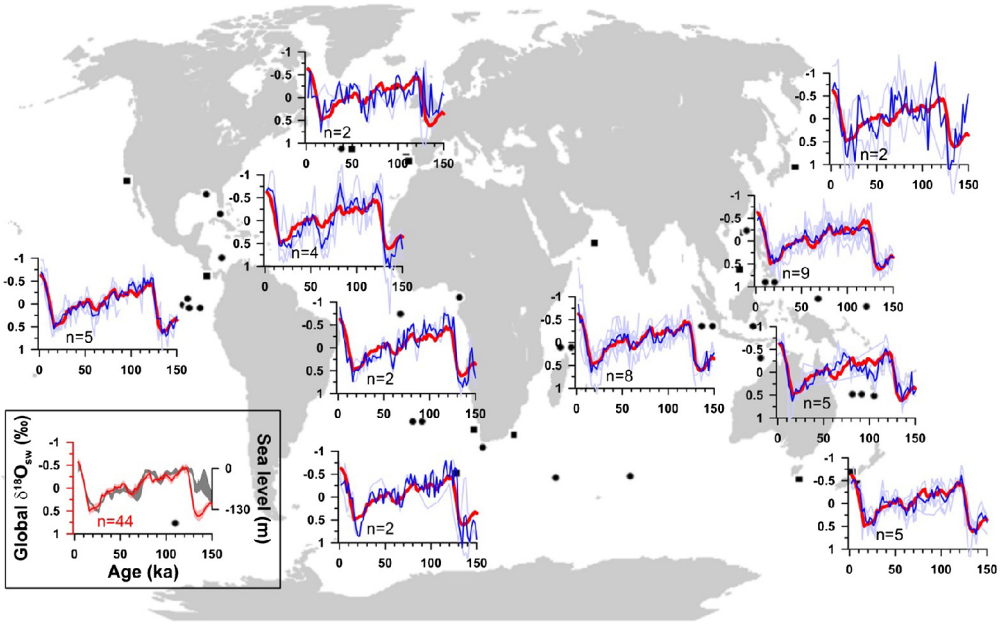

Fig. 4. Map of regional $\delta^{18}O_{sw}$ variability during the last glacial cycle. Individual (light blue) and stacked (dark blue) $\delta^{18}O_{sw}$ records over the past 150 kyr for different ocean sub-basins, divided along 30° N, 0°, and 30° S latitudes. The global $\delta^{18}O_{sw}$ stack (red) and the number of individual records for each region (n) is shown on each panel. Record locations are shown as black circles (Mg/Ca records) and squares (alkenone records) on the map. Sub-basin averages are similar to the global stack, suggesting that variability in surface ocean $\delta^{18}O_{sw}$ is relatively coherent globally and regional hydrologic effects are modest. The inset at the lower left shows that the global $\delta^{18}O_{sw}$ stack (red line, with 2σ uncertainty shading) closely resembles the sea-level record of the last glacial cycle from a global coral compilation (gray shading, 95% confidence interval) (Medina-Elizalde, 2013). (For interpretation of the references to color in this figure legend, the reader is referred to the web version of this article.)

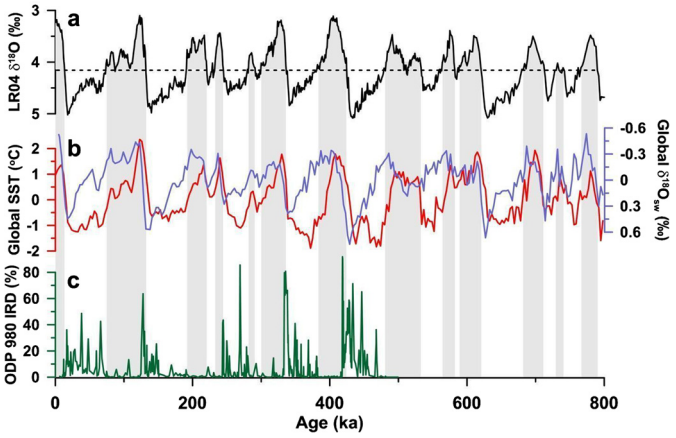

Fig. 5. Ice volume and temperature components of marine $\delta^{18}O_c$. (**a**) The LR04 benthic $\delta^{18}O$ stack, which records both global ice volume and deep ocean temperature (Lisiecki and Raymo, 2005). (**b**) Global SST (red) and $\delta^{18}O_{sw}$ (blue) stacks calculated in this study showing the temperature and ice volume components of marine $\delta^{18}O_c$. (**c**) Ice-rafted debris concentration at Ocean Drilling Program site 980 in the North Atlantic (McManus et al., 1999). The $\delta^{18}O_b$ threshold for ice-rafting (4.14‰) is demarcated by the horizontal black dashed line and vertical shading. (For interpretation of the references to color in this figure legend, the reader is referred to the web version of this article.)

temperature change by assuming that temperature linearly decreases with sea level (Siddall et al., 2003); the large lead of SST ahead of $\delta^{18}O_{sw}$ diagnosed in this study and others suggests that this assumption is unlikely to be correct, which might account for the early timing of Red Sea and Mediterranean sea level reconstructions relative to the planktic $\delta^{18}O_{sw}$ stack.

Perhaps the greatest weakness of our reconstruction is that it is based on records from the surface ocean, which are noisier than those recovered from the deep ocean. In addition, our approach considers the surface ocean to be representative of the whole ocean, which given the spurious long-term trend in the raw data is evidently not the case. These issues notwithstanding, the planktic stack exhibits several strengths relative to previous reconstructions.

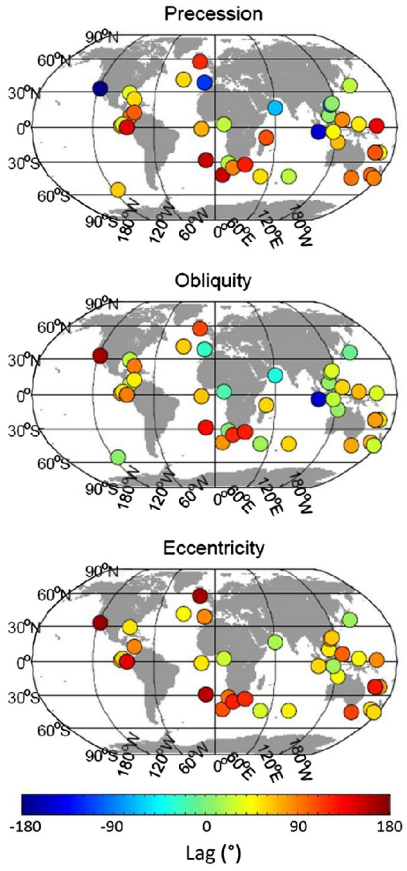

Fig. 6. Local SST-$\delta^{18}O_{sw}$ phase (in degrees) for individual records at the periods of precession (23 kyr), obliquity (41 kyr), and eccentricity (100 kyr). Positive values indicate that $\delta^{18}O_{sw}$ lags SST. Data are only shown for records spanning at least a full orbital cycle. $\delta^{18}O_{sw}$ lags SST at precession at 88% of sites, obliquity at 86% of sites, and eccentricity at all sites. Cross spectral analysis was performed using the ARAND software package (P. Howell, N. Pisias, J. Ballance, J. Baughman and L. Ochs, Brown University), which uses the Blackman–Tukey technique.

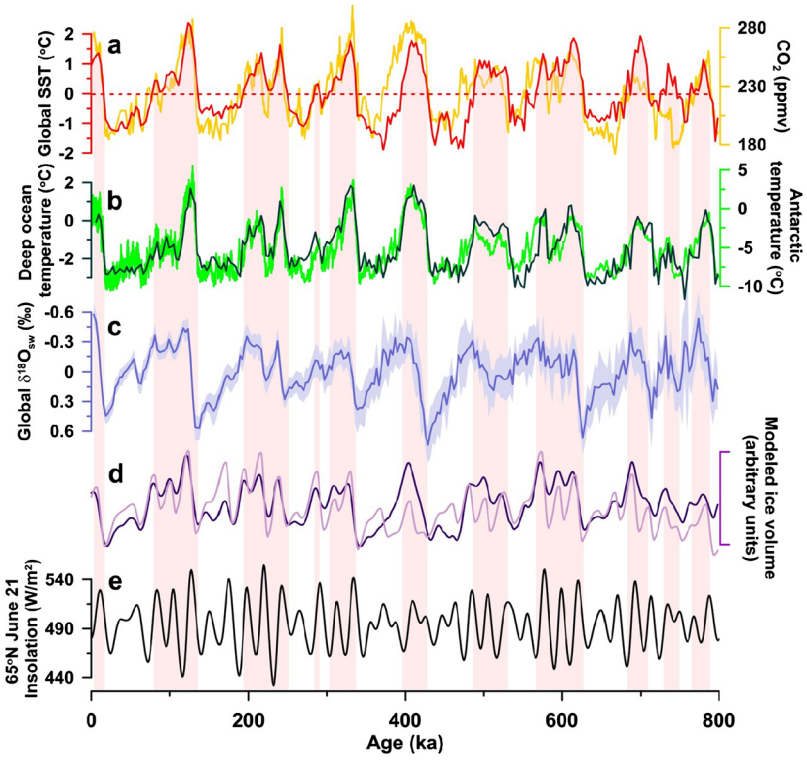

Fig. 7. Global SST, ice volume, and forcings over the past 800 kyr. (**a**) Global SST stack (red) and the ice core CO_2 record (yellow) (Luthi et al., 2008). (**b**) Antarctic temperature (light green) (Jouzel et al., 2007) and inferred bottom water temperature (dark green), calculated as the difference between the LR04 benthic stack and the planktic $\delta^{18}O_{sw}$ stack and scaled to temperature using $0.25‰ = 1\,°C$. The bottom water temperature curve is given as anomalies from the late Holocene. Note that the temperature curves are plotted on different scales. (**c**) $\delta^{18}O_{sw}$ stack with 2σ uncertainty. (**d**) Ice volume simulated with a simple linear differential model (Imbrie and Imbrie, 1980). The light purple curve was forced only with insolation and used an ice-sheet time constant of 17 kyr and an ice growth-decay asymmetry parameter of 0.6, as done by Imbrie and Imbrie (1980). The dark purple curve was forced with an unweighted average of normalized insolation and global SST, using an ice-sheet time constant of 17 kyr and no asymmetry parameter. The result is not strongly sensitive to parameter choices (Supplementary Fig. S3). (**e**) Insolation variations at 65° N on June 21 (Laskar et al., 2004). The horizontal red dashed line and vertical shading demarcate intervals when global SST is warmer than the average of the past 800 ka. Major ice growth only occurs when global SST is below this threshold. (For interpretation of the references to color in this figure legend, the reader is referred to the web version of this article.)

In particular, while most other reconstructions are derived from single sites and thus potentially susceptible to local surface or deep water hydrographic overprints, the planktic stack takes advantage of a global dataset to reduce local noise. Furthermore, the planktic stack provides an entirely empirical reconstruction of ice volume that does not depend on statistical, hydraulic, or inverse models and their associated assumptions. Lastly, the planktic stack is inherently linked to the marine isotope stratigraphy and thus can be readily compared to other marine records on the same chronology.

4. Ice volume forcings

4.1. Multivariate regression model

What drives ice sheet growth and decay over glacial cycles? We examine the time rate of change of the planktic $\delta^{18}O_{sw}$ stack to address this question, based on arguments that the rate of change, rather than ice volume itself, should most closely correspond to forcing variations (Roe, 2006). The simplest explanation for ice volume variability has long been that the rate of ice volume change is inversely related to northern high latitude summer insolation (Imbrie and Imbrie, 1980; Roe, 2006). Indeed, we also find that $d(\delta^{18}O_{sw})/dt$ exhibits a zero-lag relationship with 65° N insolation on June 21 (Roe, 2006), though the correlation is not overwhelming ($r^2 = 0.23$ for 0–800 ka and $r^2 = 0.39$ for 0–400 ka) (Fig. 10a, b), suggesting that other forcings may be at work. Note that the correlation with the integrated summer insolation forcing (Huybers, 2006) is similar ($r^2 = 0.24$ for 0–800 ka and $r^2 = 0.30$ for 0–400 ka). A multivariate regression that includes both insolation and SST improves the fit considerably ($r^2 = 0.40$ for 0–800 ka and $r^2 = 0.61$ for 0–400 ka) (Fig. 10a, c), and additionally, including $\delta^{18}O_{sw}$, as a proxy for ice volume, improves the fit still further ($r^2 = 0.49$ for 0–800 ka and $r^2 = 0.70$ for 0–400 ka) (Fig. 10a, d). This multivariate model thus suggests that ice volume variations can be largely explained by the combined influence of insolation, global temperature, and ice volume itself, with ice melting faster with stronger insolation, warmer temperatures, and when there is more ice available to melt. A warmer global climate would melt ice through sensible heating as well as through lengthening the ablation season over which insolation can act, whereas higher insolation could increase melt through direct shortwave forcing (Robinson and Goelzer, 2014; van de Berg et al., 2011). However, several intervals of rapid ice melt, particularly at terminations, are under-predicted by the model, possibly pointing to the influence of nonlinear ice dynamics at these times (Abe-Ouchi et al., 2013).

4.2. SST-$\delta^{18}O_{sw}$ cross spectral analysis

Combined insolation and temperature forcing of ice volume is also supported by cross spectral analysis of the $\delta^{18}O_{sw}$ and global SST stacks. The $\delta^{18}O_{sw}$ stack is coherent (>0.8) with SST at all orbital frequencies, but it has a smaller phase lag and larger gain relative to SST at the 23 kyr and 41 kyr periods than the 100 kyr period (Fig. 11). This faster, enhanced ice volume response is consistent with additional forcing from insolation at precession and obliquity time scales, and the lack of significant insolation forcing at the eccentricity period. It is worth noting that the 100 kyr peak remains the dominant period in the $\delta^{18}O_{sw}$ stack, in contrast

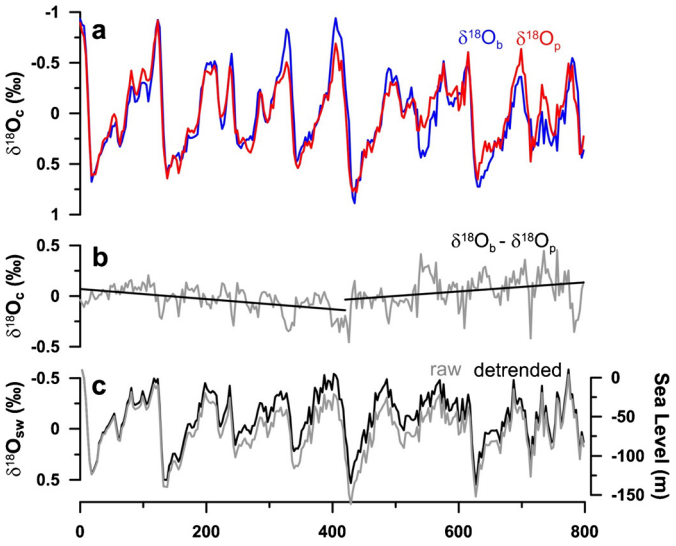

Fig. 8. Detrending the planktic $\delta^{18}O_{sw}$ stack and scaling to sea level. (**a**) The $\delta^{18}O_b$ (blue) and $\delta^{18}O_p$ (red) stacks at the sites used in this study. (**b**) The difference between the $\delta^{18}O_b$ and $\delta^{18}O_p$ stacks (gray), with trendlines from 0–430 and 430–800 ka (black). Because both records contain the same sea level imprint, the trends in the difference must reflect the influence of other processes, such as hydrological shifts. (**c**) The raw planktic $\delta^{18}O_{sw}$ stack (gray), and after removing the trends shown in panel b (black). The detrended stack was scaled to sea level with the last deglaciation spanning 130 m (Lambeck et al., 2014), equivalent to 0.008‰ per m. (For interpretation of the references to color in this figure legend, the reader is referred to the web version of this article.)

to results of a previous study that used a different technique to isolate the ice volume component from benthic $\delta^{18}O$ (Shackleton, 2000).

4.3. *Imbrie and Imbrie (1980) model*

Finally, we attempted to simulate the $\delta^{18}O_{sw}$ stack with a simple ice volume model, originally driven just using insolation by Imbrie and Imbrie (1980), but here also including global SST, similar to an earlier attempt to include CO_2 (Pisias and Shackleton, 1984). The insolation + SST model fits the data substantially better than the insolation-only model ($r^2 = 0.73$ versus 0.25) (Fig. 7c, d). In addition, whereas the insolation-only model requires an asymmetry in the ice sheet response time to orbital forcing, with slow growth and rapid decay, to produce a 100-kyr cycle (Imbrie and Imbrie, 1980), the insolation + SST model does not. This suggests that the sawtooth structure of ice volume curves may to some extent reflect the sawtooth character of global temperature forcing, rather than just a nonlinear response to the sinusoidal insolation forcing alone. This view finds some support in brief periods of rapid sea-level fall within the last glacial cycle (Lambeck et al., 2014; Siddall et al., 2008), which suggests that ice sheet growth may not necessarily be an inherently slow process.

5. Implications

5.1. *The marine $\delta^{18}O_c$ record*

The time series derived here carry several implications for Pleistocene and, to an extent, future climate change. The differences between the SST and $\delta^{18}O_{sw}$ curves show that the ice volume contribution to the marine $\delta^{18}O_c$ record varies substantially through time, confirming that this record cannot be assumed a simple ice volume proxy or that temperature and ice volume vary in a fixed ratio (Bintanja et al., 2005; Elderfield et al., 2012; Lea et al., 2002; Shackleton, 2000; Waelbroeck et al., 2002). In particular, the sawtooth structure of glacial cycles in marine $\delta^{18}O_c$ reflects the superposition of early ocean cooling and later ice volume buildup (Labeyrie et al., 1987) (Fig. 5a, b). Thus, the common notion that interglacials represent brief intervals between long glacial stages seems to apply much more to temperature than ice volume. This phasing may also point to a two-step glaciation process, in which cooling of the globe preconditions the Earth for ice growth. Such nonlinearity is reminiscent of simple threshold models of glaciation that feature multiple stable states, models that have had considerable success simulating the marine $\delta^{18}O_c$ record but for which the physical interpretation has been unclear (Paillard, 1998). Although many 100 kyr ice volume models have tried to fit the marine $\delta^{18}O_c$ record due to its

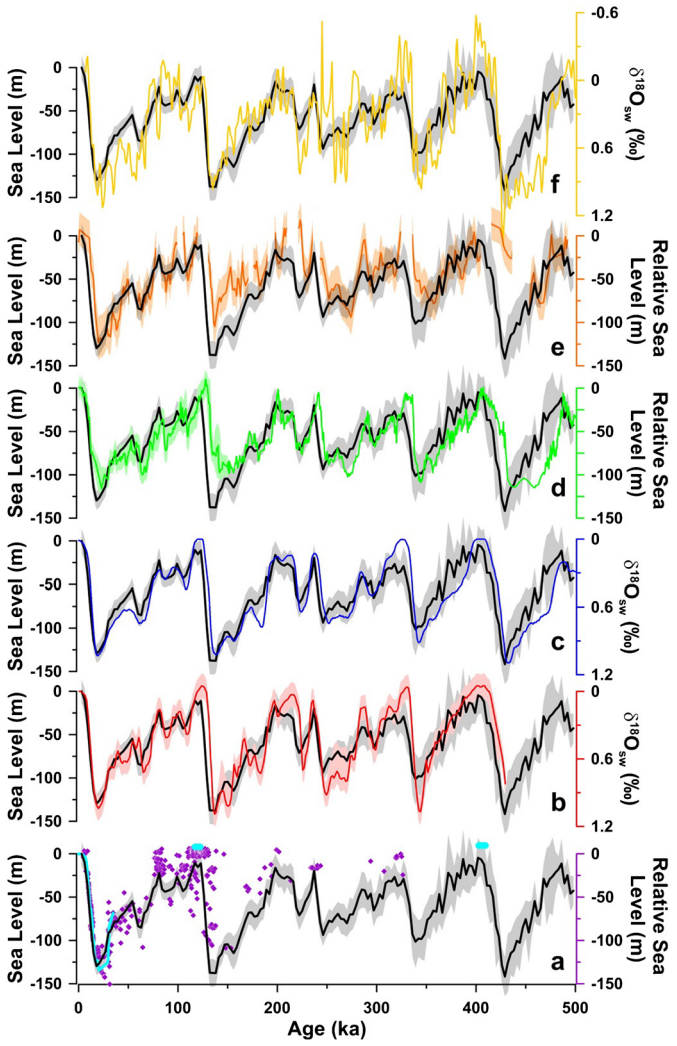

Fig. 9. The planktic $\delta^{18}O_{sw}$ sea level reconstruction (black, with 2σ uncertainty shading) compared to other reconstructions of sea level and $\delta^{18}O_{sw}$. Plots have been scaled to match variance (using 130 m per 1.0‰ for relative sea level) and aligned vertically at the Holocene. (**a**) a global compilation of uranium series-dated coral relative sea-level benchmarks (purple) (Medina-Elizalde, 2013), and global sea-level estimates (light blue) for the last deglaciation (Lambeck et al., 2014), MIS 5e (Dutton and Lambeck, 2012), and MIS 11 (Raymo and Mitrovica, 2012), (**b**) $\delta^{18}O_{sw}$ derived from a benthic $\delta^{18}O$ record calibrated to sea level benchmarks over the last glacial cycle (Waelbroeck et al., 2002), (**c**) LR04 $\delta^{18}O_{sw}$ based on inverse climate-ice sheet modeling (Bintanja et al., 2005), (**d** and **e**) sea level reconstructed from planktic oxygen isotopes from the semi-enclosed and evaporative, and thus sea-level sensitive, Red Sea (green) (Rohling et al., 2009) and Mediterranean Sea (orange) (Rohling et al., 2014) basins, and (**f**) a Mg/Ca-derived benthic $\delta^{18}O_{sw}$ record from the southwest Pacific (Elderfield et al., 2012). (For interpretation of the references to color in this figure legend, the reader is referred to the web version of this article.)

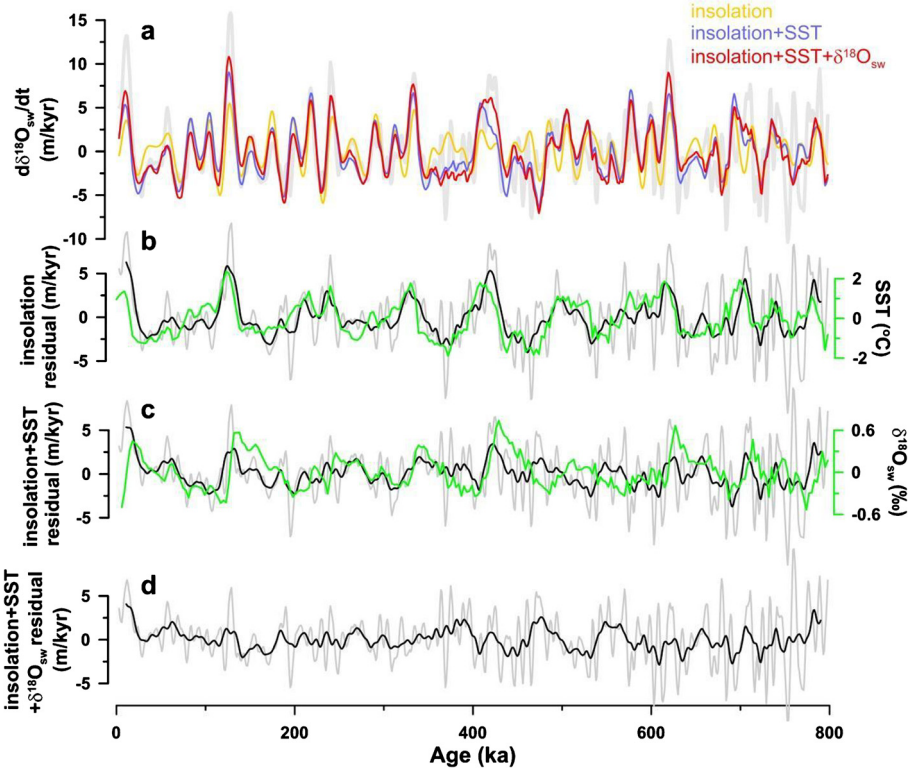

Fig. 10. Multivariate regression model of ice volume variability. (**a**) Rate of change in $\delta^{18}O_{sw}$ (gray), calculated over a running 6-kyr window and scaled to sea-level equivalent assuming 1‰ = 130 m, and regression models of $d(\delta^{18}O_{sw})/dt$ based on northern high latitude summer insolation (yellow) ($r^2 = 0.23$), insolation and global SST (blue) ($r^2 = 0.40$), and insolation, global SST, and $\delta^{18}O_{sw}$ (red) ($r^2 = 0.49$). (**b**) Residual of the insolation regression model (gray) with 17-kyr running average (black), and the global SST stack (green). (**c**) Residual of the insolation + SST regression model (gray) with 17-kyr running average (black), and the $\delta^{18}O_{sw}$ stack (green). (**d**) Residual of the insolation + SST + $\delta^{18}O_{sw}$ regression model. The three time series used in the multivariate model are nearly independent of one another, with the following correlations (r^2): insolation-SST (0.03), insolation-$\delta^{18}O_{sw}$ (0.06), SST-$\delta^{18}O_{sw}$ (0.04). (For interpretation of the references to color in this figure legend, the reader is referred to the web version of this article.)

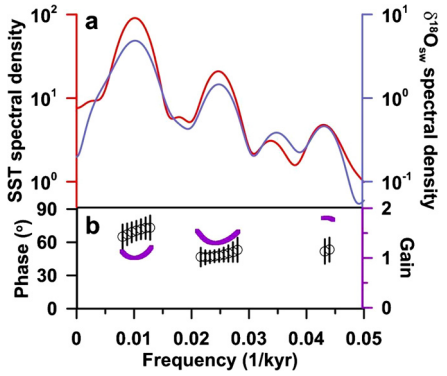

Fig. 11. Global SST-$\delta^{18}O_{sw}$ cross spectrum. (**a**) Power spectra for global SST (red) and $\delta^{18}O_{sw}$ (blue). (**b**) $\delta^{18}O_{sw}$ phase lag behind (black circles with error bars) and gain (purple) relative to SST. Gain is normalized to 1 at the 100-kyr period. Only frequencies at which $\delta^{18}O_{sw}$ is significantly coherent ($\geq$0.8) with SST are shown. Note that $\delta^{18}O_{sw}$ exhibits greater gain and shorter lags behind SST at the 23 and 41 kyr periods than at the 100-kyr period, consistent with additional forcing from insolation at precession and obliquity time scales. The $\delta^{18}O_{sw}$ lags behind SST in absolute terms are 3, 5, and 20 kyr at the precession, obliquity, and eccentricity frequencies, though we emphasize that the large lag at the 100-kyr period primarily reflects the offset between temperature and ice volume during glacial onsets rather than terminations. (For interpretation of the references to color in this figure legend, the reader is referred to the web version of this article.)

availability and superior signal/noise ratio (Abe-Ouchi et al., 2013; Imbrie and Imbrie, 1980), we propose that sea level as defined by our new $\delta^{18}O_{sw}$ record would be a more suitable model target. Furthermore, orbital tuning of $\delta^{18}O_c$ should not use ice volume response times because $\delta^{18}O_c$ reflects the combined influence of a slow ice response and potentially faster temperature signal. By the same token, the response time of ice sheets to insolation forcing may be larger than previously inferred from $\delta^{18}O_c$ (Caballero-Gill et al., 2012; Imbrie et al., 1984), although better age constraints on $\delta^{18}O_c$ or sea level records will be needed to resolve this issue.

5.2. North Atlantic ice rafting

Our finding that temperature dominates the marine $\delta^{18}O_c$ signal early in glacial cycles provides further insight into the intriguing observation that millennial-scale ice-rafting and sea surface temperature variability in the North Atlantic increase dramatically whenever $\delta^{18}O_b$ exceeds 3.5‰ (equivalent to 4.14‰ in the LR04 stack with a *Cibicidoides* species correction) (McManus et al., 1999) (Fig. 5a, c). This value was originally interpreted to represent a critical threshold in ice sheet size of $\geq$30 m sea-level equivalent. Our reconstructions show that this value is reached just after $\delta^{18}O_{sw}$ begins increasing from its interglacial minima (Fig. 5b), and may thus imply an even smaller ice volume threshold for ice rafting and increased millennial-scale SST variability. The early cooling phase of glacial cycles could also play an important role in preconditioning the system for millennial-scale instability by increasing the survivability of icebergs to sites of deepwater formation and/or facilitating a sea-ice threshold feedback.

5.3. Pleistocene glacial cycles

How did the world transition into glacial periods? The Milankovitch paradigm suggests that a strong ice sheet-albedo feedback to Northern Hemisphere summer insolation forcing initiated a large-scale, mean cooling (Imbrie and Imbrie, 1979), but this

view would need to be reconciled with our finding that ice volume lagged well behind global SST. One possibility might be that early expansion of snow and sea ice cover, both areally and seasonally, caused considerable cooling before large ice sheets grew. Alternatively, perhaps the cooling effect from the late-growing ice sheets was areally limited and had little imprint on global SST and deep ocean temperature records. In any case, because cooling preceded ice sheet growth, insolation or forcing from atmospheric CO_2, aided by relatively fast feedbacks (e.g., sea ice, vegetation, dust), seem like more plausible candidates to explain the magnitude of global cooling during an ice age cycle. However, parsing out the relative influences of these different factors is difficult due in part to current age model uncertainties in ice core and marine records. A few hints are provided by MIS 5e and 11. Temperature appears to significantly lead atmospheric CO_2 at the end of these interglacials (Cuffey and Vimeux, 2001; NEEM Community Members, 2013) (Fig. 7a), implying that orbital forcing rather than decreasing atmospheric CO_2 initiated cooling. This orbital control may also be apparent in the late Holocene; proxy data suggest that Earth surface temperature has been cooling globally for the past 5 kyr, in line with declining Northern Hemisphere insolation but in contrast to modestly rising greenhouse gas concentrations (Marcott et al., 2013).

The early cooling following peak interglacial conditions may have initiated and then been amplified by falling atmospheric CO_2 levels and fast feedbacks. Although ocean cooling has been considered to account for only a small fraction of the LGM reduction in atmospheric CO_2, since it would have been mostly canceled out by ice-sheet effects related to higher ocean salinity, smaller ocean volume, and perhaps to an extent by reduced terrestrial carbon storage (Sigman and Boyle, 2000), the large temporal offset we find in global cooling and ice growth implies that these counteracting effects would not have been synchronous. Therefore, much of the early drop in atmospheric CO_2 may be attributable to ocean cooling (Brovkin et al., 2012), a possibility supported by the close association between atmospheric CO_2 and our $\delta^{18}O_{bwt}$ reconstruction (Fig. 7a, b). Increased dust flux and iron fertilization of the Southern Ocean may then have become important for further sequestering CO_2 during the latter half of each cycle (Martínez-García et al., 2014).

In any event, as discussed above, once the globe has cooled sufficiently, ice volume begins to increase. Strikingly, global SST remains nearly constant throughout the large ice growth phase that is the dominant feature of the latter part of every glacial cycle, indicating little additional ice-temperature feedback (Fig. 7a–c). The cycle then terminates with the next large insolation increase (Fig. 7e), in the face of which these large ice sheets, sitting in the massive crustal depression caused by their weight and which, with only a minor ice margin retreat, would become instantly flooded by meltwater and seawater, would become critically unstable (Abe-Ouchi et al., 2013; Raymo, 1997), and trigger a cascade of global climate feedbacks (Denton et al., 2010; He et al., 2013; Shakun et al., 2012).

The empirical insolation-temperature-ice volume relationships inferred here may help to explain several other enigmatic features of the Pleistocene glacial cycles. A temperature threshold for Northern Hemisphere glaciation might imply that glacial cycles began when a critical level of summer cooling was reached at 2.7 Ma (Raymo et al., 1988). Such a threshold could also account for why interglacial ice volume shows little difference across the mid-Brunhes transition in the $\delta^{18}O_{sw}$ stack, despite somewhat cooler temperatures and lower CO_2 concentrations during interglacials prior to 400 ka (Fig. 7a–c). Lastly, the late Pleistocene 100-kyr and early Pleistocene 41-kyr problems center on apparent disconnects between ice volume variability and the presumed summer insolation forcing thought to drive ice sheets; there is little 100-kyr power and substantial 23-kyr power in the insolation forcing, so why is glaciation dominated by 100-kyr and 41-kyr cycles during the late and early Pleistocene? These discrepancies are typically explained by nonlinear ice-sheet responses to insolation (Imbrie and Imbrie, 1980; Paillard, 1998), alternative formulations of the insolation forcing (Huybers, 2006), or the influence of significant ice volume changes in the Southern Hemisphere (Raymo et al., 2006). If instead, however, global temperature plays an important role in driving ice volume, in addition to insolation, these problems may not be quite as large as they appear from a classical Milankovitch perspective given that temperature exhibited strong 100-kyr cyclicity during the late Pleistocene (Fig. 5b) and possibly dominant 41-kyr cyclicity during the early Pleistocene as suggested by several reconstructions (Elderfield et al., 2012; Herbert et al., 2010). This view, however, would still leave open the question of why global temperature exhibited 41 kyr cycles during the early Pleistocene and 100 kyr cycles during the late Pleistocene.

5.4. The future

Our results also speak to future greenhouse warming, if only qualitatively. First, while glacial cycles do not provide a simple analogue for future ice sheet changes associated with greenhouse warming given that part of Pleistocene ice volume variability is due to shortwave insolation forcing, our regression model suggests that another part is driven by Earth surface temperature. Second, we find strong indications of a threshold response in ice volume to global cooling, and similar ice sheet tipping points may also exist in the future with global warming. Finally, LGM time-slice simulations indicate that ice sheets and greenhouse gases were the largest radiative forcings of Ice Age climate and had comparable effects on global temperature (Köhler et al., 2010). The decoupling of SST from ice volume found here, however, suggests that temperature at many low and mid-latitude sites is not very sensitive to ice sheet size because ice volume increase during the second half of each glacial cycle did not produce additional cooling. This decoupling also suggests that glacial cooling over most of the Earth's surface was driven by atmospheric CO_2 decline and other relatively rapid responses, while the cooling effects of growing ice sheets were more localized. Thus, although greenhouse gas and ice volume changes may have had comparable effects on global temperature during Pleistocene glaciations, it is important to remember that the relative influence of these two effects varies spatially.

6. Conclusions

A global dataset of SST-corrected planktonic $\delta^{18}O$ records spanning the past 800 kyr shows: a marked coherency in $\delta^{18}O_{sw}$ variability around the surface ocean; agreement with independent estimates of deep ocean $\delta^{18}O_{sw}$ change at the LGM; and close agreement with the sea-level record over the last glacial cycle. Collectively, these observations suggest that the planktonic $\delta^{18}O_{sw}$ stack derived here dominantly reflects changes in the whole ocean isotopic composition and, by extension, the volume of ice sheets on land. Comparison with global SST variability from the same cores indicates that late Pleistocene glacial cycles were characterized by an early cooling phase followed by a later ice growth phase, suggesting that ice sheets exhibited a threshold response to cooling. Simple statistical modeling and cross-spectral analysis suggest that global temperature and insolation were both important drivers of ice volume variability; therefore, a nonlinear ice sheet response to local insolation forcing alone may not explain the 100-kyr cycle.

Collectively, our results show a close association between global SST, inferred deep ocean temperature, and atmospheric CO_2, all of which declined early in glacial cycles, whereas major ice sheet

expansion only happens later providing little additional feedback on global cooling. Terminations do not occur, however, until large ice sheets are established, suggesting that the ice sheets may have been instrumental in ending glacial cycles, if not in initiating them.

Acknowledgements

We gratefully acknowledge the researchers that developed the datasets used here, and the NOAA Paleoclimatology and Pangaea databases. JDS was supported by a NOAA Climate and Global Change Postdoctoral Fellowship and Boston College start-up funds. DWL acknowledges the support of NSF OCE-1260696. MER acknowledges the support of NSF OCE-1202632.

Appendix A. Supplementary material

Supplementary material related to this article can be found online at http://dx.doi.org/10.1016/j.epsl.2015.05.042.

References

Abe-Ouchi, A., Saito, F., Kawamura, K., Raymo, M.E., Okuno, J.i., Takahashi, K., Blatter, H., 2013. Insolation-driven 100,000-year glacial cycles and hysteresis of ice-sheet volume. Nature 500, 190–193.

Adkins, J.F., McIntyre, K., Schrag, D.P., 2002. The salinity, temperature, and $\delta^{18}O$ of the glacial deep ocean. Science 298, 1769–1773.

Bemis, B.E., Spero, H.J., Bijma, J., Lea, D.W., 1998. Reevaluation of the oxygen isotopic composition of planktonic foraminifera: experimental results and revised paleotemperature equations. Paleoceanography 13, 150–160.

Bintanja, R., van de Wal, R.S.W., Oerlemans, J., 2005. Modelled atmospheric temperatures and global sea levels over the past million years. Nature 437, 125–128.

Brovkin, V., Ganopolski, A., Archer, D., Munhoven, G., 2012. Glacial CO_2 cycle as a succession of key physical and biogeochemical processes. Clim. Past 8, 251–264.

Caballero-Gill, R.P., Clemens, S.C., Prell, W.L., 2012. Direct correlation of Chinese speleothem $\delta^{18}O$ and South China Sea planktonic $\delta^{18}O$: transferring a speleothem chronology to the benthic marine chronology. Paleoceanography 27, PA2203.

Cuffey, K.M., Vimeux, F., 2001. Covariation of carbon dioxide and temperature from the Vostok ice core after deuterium-excess correction. Nature 412, 523–527.

Denton, G.H., Anderson, R.F., Toggweiler, J.R., Edwards, R.L., Schaefer, J.M., Putnam, A.E., 2010. The last glacial termination. Science 328, 1652–1656.

Dutton, A., Lambeck, K., 2012. Ice volume and sea level during the last interglacial. Science 337, 216–219.

Dwyer, G.S., Cronin, T.M., Baker, P.A., Raymo, M.E., Buzas, J.S., Corrège, T., 1995. North Atlantic deepwater temperature change during late Pliocene and late Quaternary climatic cycles. Science 270, 1347–1351.

Elderfield, H., Ferretti, P., Greaves, M., Crowhurst, S., McCave, I.N., Hodell, D., Piotrowski, A.M., 2012. Evolution of ocean temperature and ice volume through the mid-Pleistocene climate transition. Science 337, 704–709.

Gibbons, F.T., Oppo, D.W., Mohtadi, M., Rosenthal, Y., Cheng, J., Liu, Z., Linsley, B.K., 2014. Deglacial $\delta^{18}O$ and hydrologic variability in the tropical Pacific and Indian Oceans. Earth Planet. Sci. Lett. 387, 240–251.

Hays, J.D., Imbrie, J., Shackleton, N.J., 1976. Variations in the Earth's orbit, pacemaker of the ice ages. Science 194, 1121–1132.

He, F., Shakun, J.D., Clark, P.U., Carlson, A.E., Liu, Z., Otto-Bliesner, B.L., Kutzbach, J.E., 2013. Northern Hemisphere forcing of Southern Hemisphere climate during the last deglaciation. Nature 494, 81–85.

Herbert, T.D., Peterson, L.C., Lawrence, K.T., Liu, Z., 2010. Tropical ocean temperatures over the past 3.5 million years. Science 328, 1530–1534.

Huybers, P., 2006. Early Pleistocene glacial cycles and the integrated summer insolation forcing. Science 313, 508–511.

Imbrie, J., Hays, J.D., Martinson, D.G., McIntyre, A., Mix, A.C., Morley, J.J., Pisias, N.G., Prell, W.L., Shackleton, N.J., 1984. The orbital theory of Pleistocene climate: support from a revised chronology of the marine $\delta^{18}O$ record. In: Berger, A.L., et al. (Eds.), Milankovitch and Climate. D. Reidel Publishing Company, Holland, pp. 269–305.

Imbrie, J., Imbrie, J.Z., 1980. Modeling the climatic response to orbital variations. Science 207, 943–953.

Imbrie, J., Imbrie, K.P., 1979. Ice Ages: Solving the Mystery. Harvard University Press, Cambridge, MA.

Imbrie, J., McIntyre, A., Mix, A., 1989. Oceanic response to orbital forcing in the late Quaternary: observational and experimental strategies. In: Berger, A.L., et al. (Eds.), Climate and Geo-Sciences. Kluwer Academic Publishers, pp. 121–164.

Jouzel, J., Masson-Delmotte, V., Cattani, O., Dreyfus, G., Falourd, S., Hoffmann, G., Minster, B., Nouet, J., Barnola, J.M., Chappellaz, J., Fischer, H., Gallet, J.C., Johnsen, S., Leuenberger, M., Loulergue, L., Luethi, D., Oerter, H., Parrenin, F., Raisbeck, G., Raynaud, D., Schilt, A., Schwander, J., Selmo, E., Souchez, R., Spahni, R., Stauffer, B., Steffensen, J.P., Stenni, B., Stocker, T.F., Tison, J.L., Werner, M., Wolff, E.W., 2007. Orbital and millennial Antarctic climate variability over the past 800,000 years. Science 317, 793–796.

Köhler, P., Bintanja, R., Fischer, H., Joos, F., Knutti, R., Lohmann, G., Masson-Delmotte, V., 2010. What caused Earth's temperature variations during the last 800,000 years? Data-based evidence on radiative forcing and constraints on climate sensitivity. Quat. Sci. Rev. 29, 129–145.

Labeyrie, L.D., Duplessy, J.C., Blanc, P.L., 1987. Variations in mode of formation and temperature of oceanic deep waters over the past 125,000 years. Nature 327, 477–482.

Lambeck, K., Rouby, H., Purcell, A., Sun, Y., Sambridge, M., 2014. Sea level and global ice volumes from the last glacial maximum to the Holocene. Proc. Natl. Acad. Sci. 111, 15296–15303.

Laskar, J., Robutel, P., Joutel, F., Gastineau, M., Correia, A.C.M., Levrard, B., 2004. A long term numerical solution for the insolation quantities of the Earth. Astron. Astrophys. 428, 261–285.

Lea, D.W., Martin, P.A., Pak, D.K., Spero, H.J., 2002. Reconstructing a 350 kyr history of sea level using planktonic Mg/Ca and oxygen isotope records from a Cocos Ridge core. Quat. Sci. Rev. 21, 283–293.

Lisiecki, L., Raymo, M., 2005. A Pliocene–Pleistocene stack of 57 globally distributed benthic $\delta^{18}O$ records. Paleoceanography 20, PA1003–PA1020.

Lisiecki, L.E., Lisiecki, P.A., 2002. Application of dynamic programming to the correlation of paleoclimate records. Paleoceanography 17, 1049.

Luthi, D., Le Floch, M., Bereiter, B., Blunier, T., Barnola, J.-M., Siegenthaler, U., Raynaud, D., Jouzel, J., Fischer, H., Kawamura, K., Stocker, T.F., 2008. High-resolution carbon dioxide concentration record 650,000–800,000 years before present. Nature 453, 379–382.

Marcott, S.A., Shakun, J.D., Clark, P.U., Mix, A.C., 2013. A reconstruction of regional and global temperature for the past 11,300 years. Science 339, 1198–1201.

Martin, P.A., Lea, D.W., Rosenthal, Y., Shackleton, N.J., Sarnthein, M., Papenfuss, T., 2002. Quaternary deep sea temperature histories derived from benthic foraminiferal Mg/Ca. Earth Planet. Sci. Lett. 198, 193–209.

Martínez-García, A., Sigman, D.M., Ren, H., Anderson, R.F., Straub, M., Hodell, D.A., Jaccard, S.L., Eglinton, T.I., Haug, G.H., 2014. Iron fertilization of the Subantarctic ocean during the last ice age. Science 343, 1347–1350.

McManus, J.F., Oppo, D.W., Cullen, J.L., 1999. A 0.5-million-year record of millennial-scale climate variability in the North Atlantic. Science 283, 971–975.

Meckler, A.N., Clarkson, M.O., Cobb, K.M., Sodemann, H., Adkins, J.F., 2012. Interglacial hydroclimate in the tropical West Pacific through the Late Pleistocene. Science 336, 1301–1304.

Medina-Elizalde, M., 2013. A global compilation of coral sea-level benchmarks: implications and new challenges. Earth Planet. Sci. Lett. 362, 310–318.

Mix, A.C., 1992. The marine oxygen isotope record: constraints on timing and extent of ice-growth events (120–65 ka). In: Clark, P.U., Lea, P.D. (Eds.), The Last Interglacial–Glacial Transition in North America. In: Geological Society of America Special Paper, vol. 270. Geological Society of America, Boulder, CO, pp. 19–30.

NEEM Community Members, 2013. Eemian interglacial reconstructed from a Greenland folded ice core. Nature 493, 489–494.

Paillard, D., 1998. The timing of Pleistocene glaciations from a simple multiple-state climate model. Nature 391, 378–381.

Pisias, N.G., Shackleton, N.J., 1984. Modelling the global climate response to orbital forcing and atmospheric carbon dioxide change. Nature 310, 757–759.

Raymo, M.E., 1997. The timing of major climate terminations. Paleoceanography 12, 577–585.

Raymo, M.E., Lisiecki, L.E., Nisancioglu, K.H., 2006. Plio-Pleistocene ice volume, Antarctic climate, and the global $\delta^{18}O$ record. Science 313, 492–495.

Raymo, M.E., Mitrovica, J.X., 2012. Collapse of polar ice sheets during the stage 11 interglacial. Nature 483, 453–456.

Raymo, M.E., Ruddiman, W.F., Froelich, P.N., 1988. Influence of late Cenozoic mountain building on ocean geochemical cycles. Geology 16, 649–653.

Robinson, A., Goelzer, H., 2014. The importance of insolation changes for paleo ice sheet modeling. Cryosphere 8, 1419–1428.

Roe, G., 2006. In defense of Milankovitch. Geophys. Res. Lett. 33, L24703.

Rohling, E.J., Foster, G.L., Grant, K.M., Marino, G., Roberts, A.P., Tamisiea, M.E., Williams, F., 2014. Sea-level and deep-sea-temperature variability over the past 5.3 million years. Nature 508, 477–482.

Rohling, E.J., Grant, K., Bolshaw, M., Roberts, A.P., Siddall, M., Hemleben, C., Kucera, M., 2009. Antarctic temperature and global sea level closely coupled over the past five glacial cycles. Nat. Geosci. 2, 500–504.

Schrag, D.P., Adkins, J.F., McIntyre, K., Alexander, J.L., Hodell, D.A., Charles, C.D., McManus, J.F., 2002. The oxygen isotopic composition of seawater during the last glacial maximum. Quat. Sci. Rev. 21, 331–342.

Shackleton, N.J., 2000. The 100,000 year Ice-Age cycle identified and found to lag temperature, carbon dioxide and orbital eccentricity. Science 289, 1897–1902.

Shakun, J.D., Clark, P.U., He, F., Marcott, S.A., Mix, A.C., Liu, Z., Otto-Bliesner, B., Schmittner, A., Bard, E., 2012. Global warming preceded by increasing carbon dioxide concentrations during the last deglaciation. Nature 484, 49–54.

Siddall, M., Rohling, E.J., Almogi-Labin, A., Hemleben, C., Meischner, D., Schmelzer, I., Smeed, D.A., 2003. Sea-level fluctuations during the last glacial cycle. Nature 423, 853–858.

Siddall, M., Rohling, E.J., Arz, H.W., 2008. Convincing evidence for rapid ice sheet growth during the last glacial period. Pages Newsl. 16, 15–16.

Sigman, D.M., Boyle, E.A., 2000. Glacial/interglacial variations in atmospheric carbon dioxide. Nature 407, 859–869.

Sosdian, S., Rosenthal, Y., 2009. Deep-sea temperature and ice volume changes across the Pliocene–Pleistocene climate transitions. Science 325, 306–310.

van de Berg, W.J., van den Broeke, M., Ettema, J., van Meijgaard, E., Kaspar, F., 2011. Significant contribution of insolation to Eemian melting of the Greenland ice sheet. Nat. Geosci. 4, 679–683.

Waelbroeck, C., Labeyrie, L., Michel, E., Duplessy, J.C., McManus, J.F., Lambeck, K., Balbon, E., Labracherie, M., 2002. Sea-level and deep water temperature changes derived from benthic foraminifera isotopic records. Quat. Sci. Rev. 21, 295–305.

Winograd, I.J., Coplen, T.B., Landwehr, J.M., Riggs, A.C., Ludwig, K.R., Szabo, B.J., Kolesar, P.T., Revesz, K.M., 1992. Continuous 500,000-year climate record from vein calcite in Devils Hole, Nevada. Science 258, 255–260.